SCIENTIFIC REPORTS

OPEN

SUBJECT AREAS:
ELECTROCATALYSIS
SYNTHESIS AND PROCESSING
ELECTRONIC MATERIALS
ENERGY TRANSFER

Received
18 October 2012

Accepted
11 January 2013

Published
4 February 2013

Correspondence and requests for materials should be addressed to G.-R.L. (ligaoren@mail.sysu.edu.cn)

Hierarchical Pd-Sn Alloy Nanosheet Dendrites: An Economical and Highly Active Catalyst for Ethanol Electrooxidation

Liang-Xin Ding, An-Liang Wang, Yan-Nan Ou, Qi Li, Rui Guo, Wen-Xia Zhao, Ye-Xiang Tong & Gao-Ren Li

MOE Laboratory of Bioinorganic and Synthetic Chemistry, KLGHEI of Environment and Energy Chemistry, School of Chemistry and Chemical Engineering, Instrumental Analysis & Research Center, Sun Yat-sen University, Guangzhou 510275, P. R. China.

Hierarchical alloy nanosheet dendrites (ANSDs) are highly favorable for superior catalytic performance and efficient utilization of catalyst because of the special characteristics of alloys, nanosheets, and dendritic nanostructures. In this paper, we demonstrate for the first time a facile and efficient electrodeposition approach for the controllable synthesis of Pd-Sn ANSDs with high surface area. These synthesized Pd-Sn ANSDs exhibit high electrocatalytic activity and superior long-term cycle stability toward ethanol oxidation in alkaline media. The enhanced electrocataytic activity of Pd-Sn ANSDs may be attributed to Pd-Sn alloys, nanosheet dendrite induced promotional effect, large number of active sites on dendrite surface, large surface area, and good electrical contact with the base electrode. Because of the simple implement and high flexibility, the proposed approach can be considered as a general and powerful strategy to synthesize the alloy electrocatalysts with high surface areas and open dendritic nanostructures.

Pt has been widely studied as electrocatalysts for the oxidation of small organic molecules, such as methanol and ethanol, for direct alcohol fuel cells (DAFCs) that are regarded as promising future power sources[1–3]. However, the high cost and limited supply of Pt constitute a major barrier to the wide application of Pt-based electrocatalysts[4–6], and accordingly Pt-free electrocatalysts have attracted much interest[7]. It has shown that Pd is a promising electrocatalyst because it is much cheaper than Pt and is high electroactive for small organic molecule oxidation in basic media[8–17]. Meanwhile, the addition of a second element, such as transition metal Sn, to Pd can obviously improve the overall electrocatalytic activities of Pd because of the bimetallic promotional effect[18]. Besides the components, the sizes and surface morphologies of electrocatalysts are also crucial for their catalytic activities[19]. Recently, the tailored design and synthesis of Pd-based alloy electrocatalysts have attracted much attention because of their low cost and superior catalytic activities[20,21].

Nanodendrites are an important class of materials that are highly attractive due to their high surface-area-to-volume ratio, high degree of connectivity, high porousness, and a large number of edges and corner atoms[22]. These characteristics make the nanodendrites highly useful for a number of applications including catalysis[23], chemical sensing[24], and surface enhanced Raman scattering[25]. In terms of their catalytical use, the organization of Pd-based materials into nanodendrites is highly attractive[26,27]. Based on the reports in literatures[28], most of the nanodendrites are constructed by nanoparticles (0D) or nanorods (1D), and the dendrites constructed by 2D nanosheets are not often reported, especially for Pd-based alloy materials. Compared with 0D and 1D nanostructures, the 2D nanosheets have much richer physical and chemical properties. For example, the relativistic nature of charge carriers in graphene nanosheets may lead to the breakthroughs in future electronic devices[29]. Therefore, the Pd-based alloy nanosheet dendrites (ANSDs) as new catalysts will attract much interest because of the special conjunct effects of alloys, nanosheets, and dendritic structures. However, up to now, it still remains a great challenge to find a method to fabricate the well defined Pd-based ANSDs.

Based on the above considerations, we synthesized Pd-Sn ANSDs with low Pd content via electrodeposition, which has the following merits: (*i*) the second metal element, such as Sn, can be easily co-deposited with Pd to form Pd-Sn alloys, (*ii*) the Pd-Sn ANSDs are easily synthesized, and various Pd-Sn alloy dendrites can be well controlled, (*iii*) the Pd-Sn ANSDs can directly grow on conductive substrate in a good solid contact that can

largely enhance the conductivity. The Pd-Sn ANSDs are ideally suited for high efficient electrochemical reactions because they have large surface areas, large number of edges and corner atoms, continuous nanosheet networks, and numerous pores. The results reported in this paper prove that the fabricated Pd-Sn ANSDs exhibit remarkable electrocatalytic activity for ethanol oxidation. This study will be highly interest and important for the development of low-cost Pd-based alloy electrocatalysts.

Results

SEM images of the synthesized Pd-Sn ANSDs are shown in Figures 1(a–b), which show the symmetrical dendritic nanostructures were fabricated. The leaf-like nanosheets are well aligned on both sides of stems. The thicknesses of these nanosheets are about 50 nm, and their lengths are in the range of 10∼12 μm. The overall lengths of Pd-Sn ANSDs are about 100∼150 μm. The continuous networks and highly porous structures are clearly seen in Pd-Sn ANSDs, and they will provide fast charge transfer and electroactive species transport, respectively, which will lead to the excellent catalytic activity for these materials. The elements of Pd and Sn are clearly seen in EDS spectrum in Figure S2a, which shows Pd content in Pd-Sn ANSDs is as low as 11.36 at%. The Pd-Sn alloy phases are seen in XRD pattern in Figure S2b, which shows the successful synthesis of Pd-Sn alloys. In addition, a small peak of SnO is detected, and this may be attributed to the partial oxidation of Sn. The electronic structure of the surface of Pd-Sn ANSDs is evaluated by XPS spectra (Figure S3a). The Pd 3*d* levels of Pd-Sn ANSDs exhibit binding energies of 340.80 eV ($3d_{3/2}$) and 335.55 eV ($3d_{5/2}$), which are positively shifted ∼0.4 eV compared with those of Pd metal (340.40 eV ($3d_{3/2}$), 335.15 eV ($3d_{5/2}$))[30]. This result implies that the addition of Sn has an influence on the electronic structure of Pd in Pd-Sn ANSDs. Figure S3b shows the Sn 3*d* regions of Pd-Sn ANSDs. The peak centered at 485.0 eV, in agreement with the literature data[31], can be assigned to a "quasimetallic" Sn species with a binding energy slightly greater than that of pure metal Sn. The above results comfirm the electron interactions involving Pd and Sn atoms within Pd-Sn ANSDs. Considering the applied potentials in this study, the peak at 486.9 eV in XPS spectrum can be assigned to Sn^{2+} species[32], which comes from the partial oxidation of Sn (SnO). This is in accordance with the result of XRD.

TEM images of the typical branch in Pd-Sn ANSDs are shown in Figures 1(c–d), which also show leaf-like nanosheets are orderly aligned on both sides of the stem. HRTEM image was measured as shown in Figure 1e, which displays the lattice fringes of a typical nanosheet in Pd-Sn ANSDs, indicating the nanosheet possesses polycrystalline structure. These interplanar spacings in Figure 1e are determined to be 0.32, 0.30, and 0.22 nm, which are identical with (200) and (202) facet distances of $PdSn_3$ phase and (204) facet

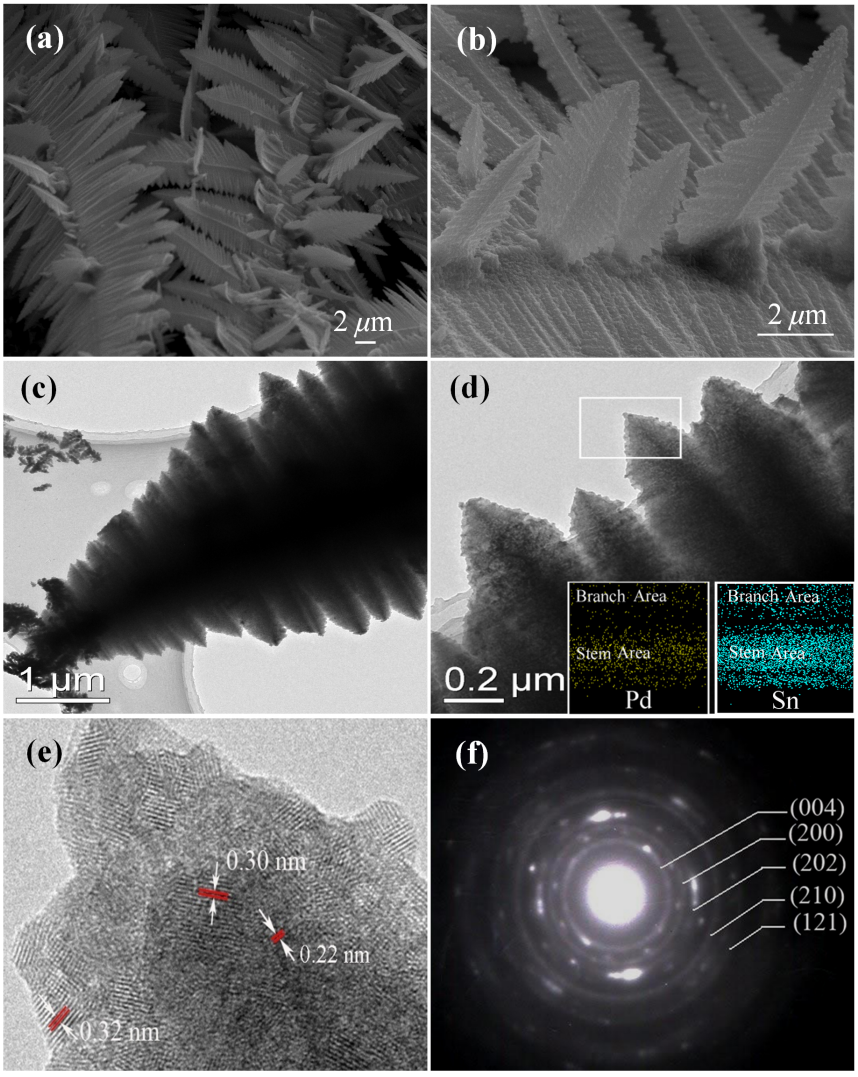

Figure 1 | SEM images of Pd-Sn ANSDs: (a) low magnification, (b) high magnification. (c–d) TEM images of Pd-Sn ANSDs with different magnifications (EDS maps, insets in (d)), (e) HRTEM image, and (f) SAED of Pd-Sn ANSDs.

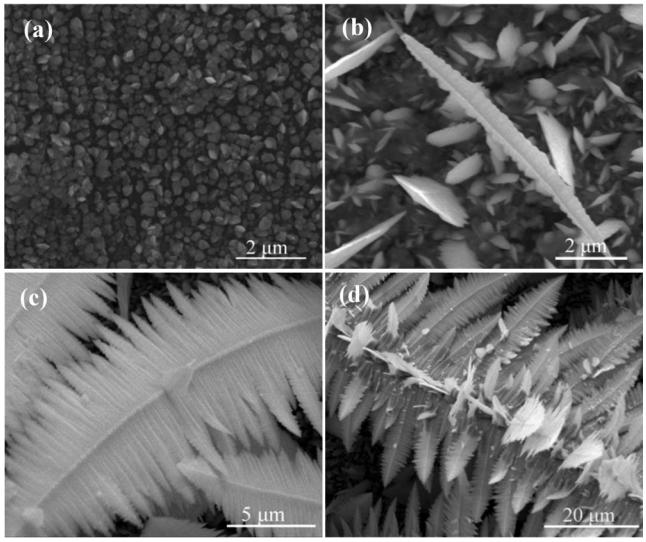

Figure 2 | SEM images of Pd-Sn deposits prepared in 0.02 M $SnCl_2$ + 0.0025 M $PdCl_2$ + 0.01 M $C_6H_{11}O_7Na$ + 3.0 M HCl at 1.5 mA/cm² for various deposition time: (a) 5 min, (b) 25 min, (c) 45 min, (d) 60 min.

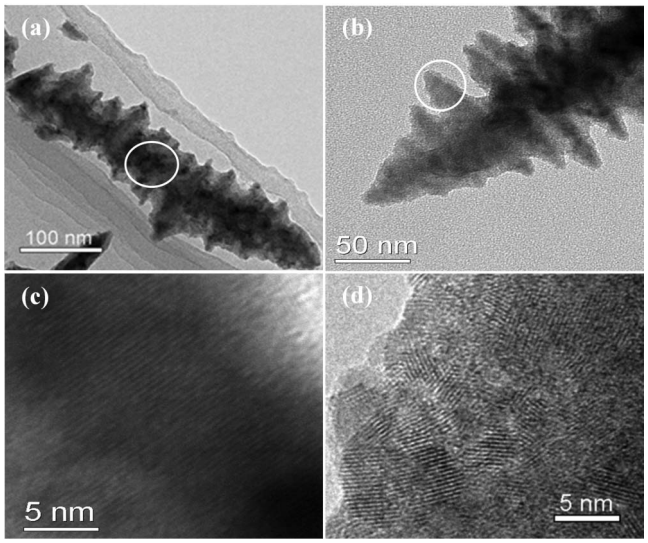

Figure 3 | TEM images of (a) Pd-Sn nanorod with small sawtoothes and (b) Pd-Sn ANSD, (c) HRTEM of the stem in Pd-Sn sample in (a), (d) HRTEM of the branch in Pd-Sn sample in (b).

distance of $PdSn_2$ phase, respectively. The SAED pattern is shown in Figure 1f, which also shows the polycrystalline structure of Pd-Sn alloy nanosheet. The EDS maps were measured to study the elemental distributions of Pd and Sn metals in dendrites. The images in Figure 1d (insets) reveal that the contents of Pd and Sn in stem areas are much higher than those in branch areas, which may be attributed to the longer growth time of stems than that of branches. The elemental distributions in stem and branch areas are uniformly dispersed, respectively. As we all know, the elemental distribution represents the particle distribution[33]. So the above results indicate highly dispersed Pd-Sn alloy nanocrystals in dendrites, which will provide plenty of interface areas with high electroactive sites.

To understand the growth process of Pd-Sn ANSDs, various Pd-Sn alloy samples were fabricated in solution of 0.02 M $SnCl_2$ + 0.0025 M $PdCl_2$ + 0.01 M $C_6H_{11}O_7Na$ + 3.0 M HCl as a function of deposition time such as 5, 25, 45, and 60 min, respectively, and they are shown in Figure 2. When electrodeposition time is 5 min, Pd-Sn alloy nanoparticles of 200~300 nm are obtained as shown in Figure 2a. With deposition time increasing to 25 min, Pd-Sn alloy nanorods with small sawtoothes can be vaguely seen as shown in Figure 2b, and their diameters and lengths are about 600 nm and 9.2 μm, respectively. When deposition time is 45 min, Pd-Sn ANSDs are definitely formed, and their lengthes are about 30 μm as shown in Figure 2c. When deposition time is 60 min, Pd-Sn ANSDs consist of much more branches and their lengths are up to 100 μm as shown in Figure 2d. From these SEM images, one can figure out that there is a tendency that Pd-Sn alloy nanostructure grows more and more complex. At the initial formation stage, the irregular nanoparticles are usually produced. With evolution process going along, the Pd-Sn alloy nanoparticles will become rod-like nanostructures with small sawtoothes and gradually form the larger dendritic nanostructures.

TEM measurements also support the proposed formation process of Pd-Sn ANSDs. As shown in Figure 3a, Pd-Sn alloy nanorods with small sawtoothes are formed in the early growth stage of nanodendrite. Then Pd-Sn nanodendrites are evolved as shown in Figure 3b. The single-crystal structure of stem is proved by HRTEM image as shown in Figure 3c, which proves the formation of stem in the early growth stage is induced by anisotropic growth of nuclei. HRTEM image in Figure 3d shows the branch in Pd-Sn ANSDs is polycrystalline, and accordingly the growth of branch may be attributed to nuclei moving in random walk trajectories and sticking on a seed particle with tips growing preferentially[34,35].

Based on the above results of CV, SEM and TEM, the steps involved in seeding growth of Pd-Sn ANSDs are illustrated in Figure 4, and the formation mechanism is expressed as follows. Pd^{2+} and Sn^{2+} ions in solution are firstly electroreduced, and then Pd-Sn alloys will be immediately formed by electrochemical mixing the reduced Pd and Sn atoms. The electrodeposition generally gives rise to the isolated nuclei on substrate, and these nuclei are randomly and uniformly distributed (Figure 2a). With deposition time going along, the isolated nuclei will evolve to Pd-Sn alloy nanorods with small sawtoothes (Figure 2b) that will act as growth centers or

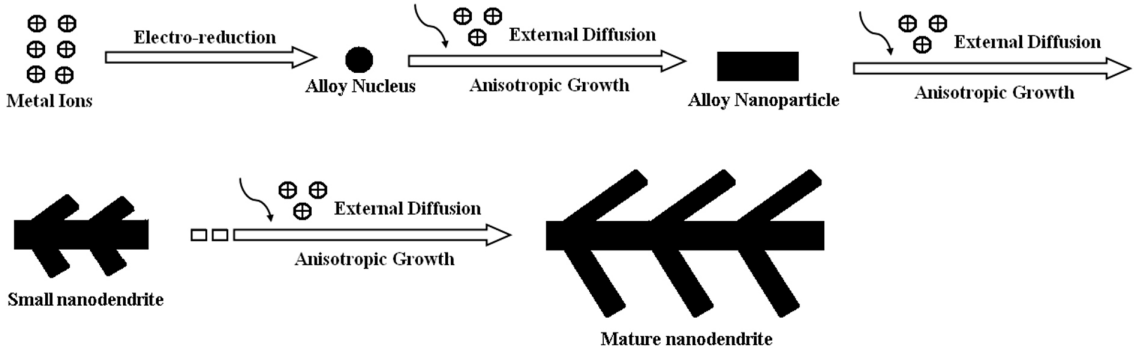

Figure 4 | The illustration for the formation process of Pd-Sn ANSDs.

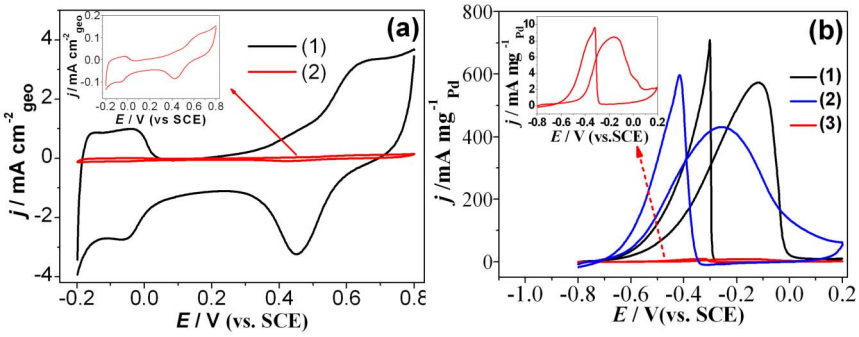

Figure 5 | (a) CVs of (1) Pd-Sn ANSDs and (2) out-of-order Pd-Sn nanoparticles recorded in the deaerated 0.5 M H_2SO_4 at 50 mV/s, (b) CVs of (1) Pd-Sn ANSDs, (2) commercial Pd/C catalyst, and (3) Pd-Sn ANPs recorded in 1.0 M C_2H_5OH + 1.0 M KOH at 50 mV/s.

seeds[35,36]. These structures follow an adapted diffusion-limited growth pattern model, where particles move in random walk trajectories and anisotropically stick on a seed particle with tips growing preferentially. So the subsequent growth of Pd-Sn alloy crystals would preferentially deposit on the preformed nuclei rather than on the substrate surface, which is possibly due to the relatively high activation energy for surface reaction[36,37]. In other words, in following electrochemical reduction process, the newly deposited Pd-Sn alloy nuclei will act as the local cathode[36]. When the seeds reach certain size (about 500 atoms), the electroreductions of Pd^{2+} and Sn^{2+} ions will be accelerated through the autocatalytic reduction process, which would be facilitated to a highly anisotropic mode to form dendritic feelers on the surface of each cluster[37]. In the end, the integrated Pd-Sn ANSDs will be synthesized through the gradual and continued electrodeposition of Pd-Sn alloys onto the deposited nuclei (Figures 2c and 2d). The diffusion-limited aggregation model is evidenced by structural dependence of dendrite on the temperature as studied by comparing SEM images of Pd-Sn alloy deposits at 90, 60, and 25°C (Figure S4). Pd-Sn alloy nanoparticles (ANPs) are produced at 90 and 60°C, while the dendrites are produced at 25°C. With temperature decreasing, the diffusion rate of ions in solution becomes slower, and this leads to the anisotropic growth of Pd-Sn NSDs at 25°C because of the diffusion-limited aggregation.

Discussion

The nanosheet dendrite structure endows the synthesized Pd-Sn NSDs with some advantageous properties: large electrochemically active surface area (EASA) and porous structures, which are desired in their catalytic applications. The EASA of Pd-Sn ANSDs (Pd loading is 196 $\mu g/cm^2$) was studied based on hydrogen adsorption using cyclic voltammetry measurement. Figure 5a shows CV of Pd-Sn ANSDs and ANPs in the deaerated H_2SO_4 solution (0.5 M) at 50 mV/s. Compared with Pd-Sn ANPs (Pd loading is 221 $\mu g/cm^2$, SEM image is shown in Figure S5), Pd-Sn ANSDs exhibit much larger adsorption/desorption peaks although they have lower Pd loading, indicating much larger EASA for Pd-Sn ANSDs. The above results also indicate higher proportional Pd is electrochemically available on the surfaces of Pd-Sn ANSDs than on the surfaces of Pd-Sn ANPs, and accordingly such Pd-Sn ANSDs largely increase the electrtoactive sites. In addition, compared with Pd-Sn ANPs, the Pd-Sn ANSDs can highly improve the transmission of electron and the diffusion of electroactive species because of their nanosheet networks and porous structures.

In order to illuminate superior catalytic properties and potential applications of the synthesized Pd-Sn ANSDs, the comparison of electrochemical properties of Pd-Sn ANSDs and Pd-Sn ANPs was performed. CV curves of Pd-Sn ANSDs *vs* ANPs were measured in solution of 1.0 M C_2H_5OH + 1.0 M KOH at 50 mV/s as shown in Figures 5b(1) and 5b(3), respectively. For Pd-Sn ANSDs, the onset potential of ethanol oxidation is about −0.474 V, which is 57 mV more negative than −0.417 V obtained on Pd-Sn ANPs, indicating a significant enhancement in the kinetics of ethanol oxidation on Pd-Sn ANSDs. The mass specific peak current densities on Pd-Sn ANSDs and ANPs in positive-going potential scan are 576 and 8.52 mA mg^{-1}_{Pd}, respectively, and accordingly the Pd-Sn ANSDs exhibit ~67 times higher catalytic activity than Pd-Sn ANPs. The above results show Pd-Sn ANSDs own much higher catalytic activity than Pd-Sn ANPs. In addition, the Pd-Sn ANSDs exhibit ~1.33 times higher catalytic activity than the commercial Pd/C catalyst (JM) and ~8.8 times higher catalytic activity than Pd nanowire arrays reported in literature[9]. Figure S6 shows the chronoamperometric curves of

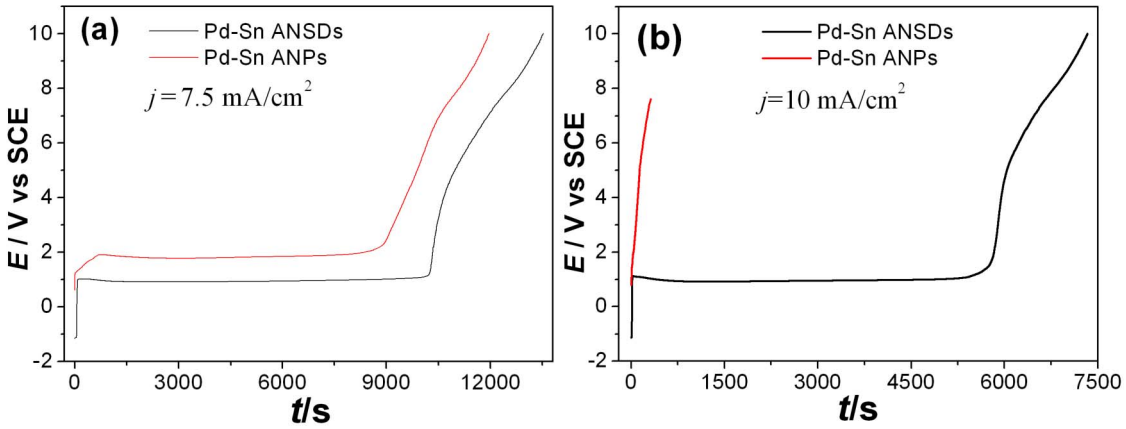

Figure 6 | **The chronopotentiometric curves of Pd-Sn ANSDs and ANPs in 1.0 M C_2H_5OH + 1.0 M KOH at room temperature at (a) 7.5 and (b) 10 mA/cm².**

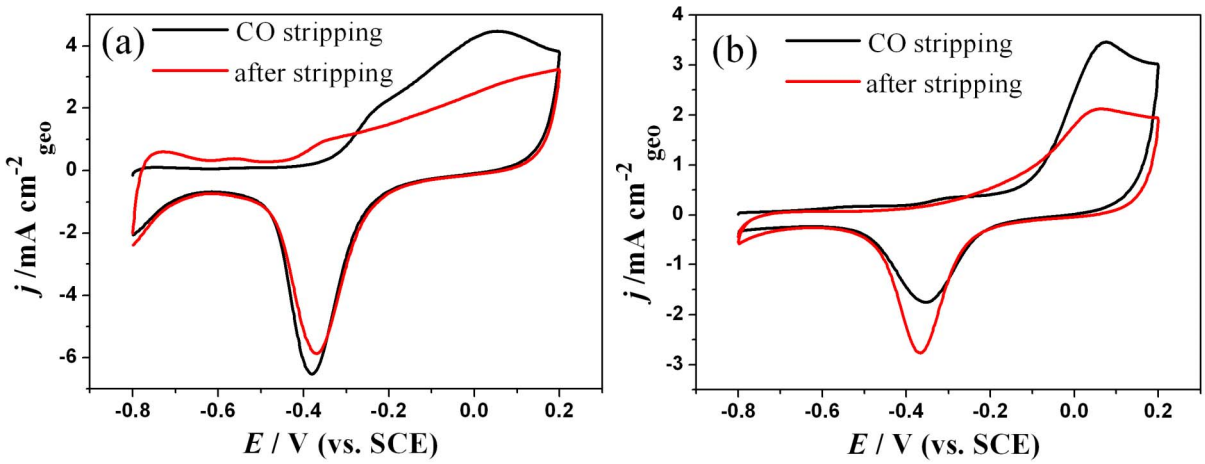

Figure 7 | **The CO stripping voltammograms of (a) Pd-Sn ANSDs and (b) Pd-Sn ANPs in 1.0 M KOH at 50 mV/s.**

Pd-Sn ANSDs and ANPs in solution of 1.0 M C_2H_5OH + 1.0 M KOH at −0.20 V for 800 s, and it also shows the Pd-Sn ANSDs have much higher catalytic activity than Pd-Sn ANPs. The chronopotentiometric curves of ethanol electrooxidation on Pd-Sn ANSDs *vs* ANPs at different current densities are shown in Figures 6a and 6b. When the current density is 7.5 mA/cm^2, in the early stage, the potential keeps stability with polarization time increasing as shown in Figure 6a. Once the active sites are blocked by ethanol by-products formed during the oxidation, they will lose activity, and in order to maintain the applied current (7.5 mA/cm^2), the electrodes are shifted to high potentials where the oxygen evolution reaction takes place[37]. The sustained stability time of Pd-Sn ANSDs is about 10214s, which is longer than 8604 s for Pd-Sn ANPs. Moreover, the polarization potential of Pd-Sn ANSDs are lower than that of Pd-Sn ANPs. When current density is increased to 10 mA/cm^2, Pd-Sn ANPs were poisoned immediately, but Pd-Sn ANSDs exhibit much longer sustaining stability time as shown in Figure 6b. Therefore, Pd-Sn ANSDs show much higher ability for counteracting catalyst deterioration and much higher stability than Pd-Sn ANPs.

In order to evaluate the rate of surface poisoning Pd-Sn ANSDs, the CO stripping experiments on Pd-Sn ANSDs *vs* Pd-Sn ANPs in solution of 1.0 M KOH at 50 mV/s are carried out and the results are shown in Figures 7a and 7b, respectively. The onset potential of CO oxidation on Pd-Sn ANSDs (−0.33 V) is obviously more negative than that on Pd-Sn ANPs (−0.13 V) and is also more negative than that on Pd/C catalyst (−0.19 V)[38]. This means that Pd-Sn ANSDs can facilitate the removal of CO from the surface of catalyst. This result is favorable to explain higher catalytic activity of Pd-Sn ANSDs for ethanol electrooxidation than Pd-Sn ANPs and Pd/C catalyst. In addition, after CO stripping, the adsorption/desorption peaks of hydrogen are clearly seen for Pd-Sn ANSDs and CO adsorption peak is almost not observed as shown in Figure 7a. However, for Pd-Sn ANPs, the CO adsorption peak is still seen after CO stripping, and the adsorption/desorption peaks of hydrogen are almost not seen as shown in Figure 7b. Therefore, compared with Pd-Sn ANPs, the Pd-Sn ANSDs exhibit great ability to overcome CO poisoning during ethanol electrooxidation.

Here we also examined the effects of surface morphologies of Pd-Sn alloy nanodendrites on the electrocatalytic activity for the ethanol electrooxidation reaction. In this study, three kinds of typical Pd-Sn alloy dendritic nanostructures were compared, namely, Pd-Sn ANSDs, Pd-Sn alloy nanoparticle dendrites with nanoparticle sizes of 150∼200 nm (Pd-Sn ANPDs-1), and Pd-Sn alloy nanoparticle dendrites with nanoparticle sizes of ∼75 nm (Pd-Sn ANPDs-2), and their SEM images are shown in Figure 1, Figure S7, and Figure S8, respectively. CVs of various Pd-Sn alloy nanodendrites with the same Pd loading of 196 μg/cm^2 in the deaerated H_2SO_4 solution (0.5 M) at a scan rate of 50 mV/s are shown in Figure 8a, which shows Pd-Sn ANSDs have the biggest EASA and Pd-Sn ANPDs-1 and ANPDs-2 have much smaller EASA. Figure 8b shows CVs of ethanol electrooxidation in 1.0 M C_2H_5OH + 1.0 M KOH on the various Pd-Sn dendritic nanostructures. The anodic peak current of Pd-Sn ANSDs in the forward scan is 576 mA mg^{-1}_{Pd}, which is much higher than those of Pd-Sn ANPDs-1 and ANPDs-2. The above results clearly demonstrate the electrocatalytic activity of Pd in alloys

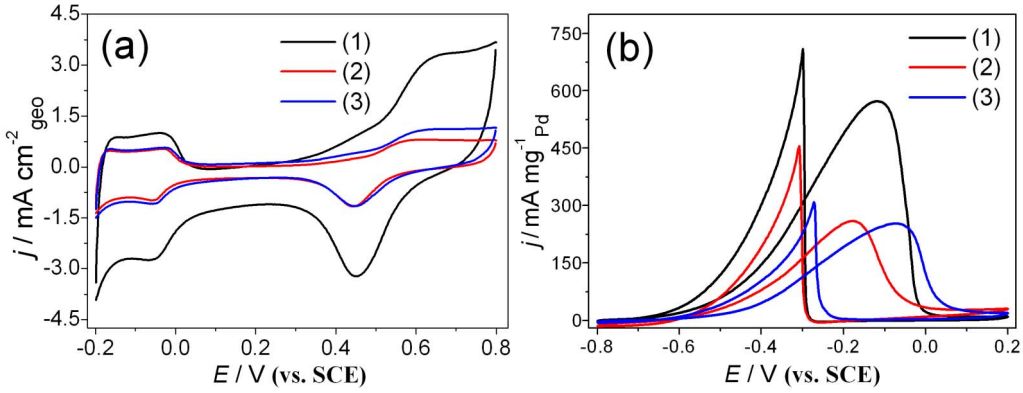

Figure 8 | (a) CVs in the deaerated 0.5 M H_2SO_4 solution and (b) CVs of ethanol oxidation in 1.0 M C_2H_5OH + 1.0 M KOH on (1) Pd-Sn ANSDs, (2) Pd-Sn ANPDs-1 and (3) Pd-Sn ANPDs-2 electrodes with Pd loading of 196 μg/cm^2.

depend strongly on the structure of nanodendrites. In the case of Pd-Sn ANSDs, the relatively large gaps or pores between nanosheets can act as the high effective transportation channels to and from the electrode/electrolyte interface for the liquid fuel and products formed during the electrooxidation of ethanol. In addition, the special thin nanosheet structures in nanodendrites can provide faster electron transmission and higher utilization rate of electrocatalyst. These superior characteristics appear to be supported by the high electrocatalytic activity of Pd-Sn ANSDs electrode in comparison to those of Pd-Sn ANDs-1 and ANPDs-2 electrodes.

In summary, a rapid and efficient electrodeposition route to synthesize the low-cost Pd-Sn ANSDs with superior performance was developed. The high electrocatalytic activities of Pd-Sn ANSDs can be attributed to the special conjunct effects of Pd-Sn alloys, special effects of 2D nanosheets, and dendritic structure-induced promotional effects (such as large specific surface area, fast charge transmission, high transport rate of active species, and large number of edges and corner atoms). Given their low cost and ease to fabricate in large-area, the Pd-Sn ANSDs as catalysts with high performance hold promise for DAFCs in the future. In addition, Pd-Sn ANSDs are also expected to possess other scientific and technological applications, such as surface plasmon-related research topics, design of novel chemical sensors, and much more.

Methods

Electrodeposition of Pd-Sn alloys was studied by cyclic voltammograms (CVs) as shown in Supporting Information, and it has been proved to be an efficient route for the fabrication of Pd-Sn alloys. The electrochemical deposition of bimetallic Pd-Sn alloy electrocatalysts with dendritic nanostructures was carried out in solutions of 0.01 M $SnCl_2$ + 0.0025 M $PdCl_2$ + 3.0 M HCl + 0.01 M NH_4Cl, 0.01 M $SnCl_2$ + 0.0025 M $PdCl_2$ + 2.0 M HCl + 0.02 M citric acid, and 0.01 M $SnCl_2$ + 0.0025 M $PdCl_2$ + 1.0 M HCl + 0.02 M $CH_2OH(CHOH)_4COONa$, respectively, on Ti substrates by galvanostatic electrolysis at room temperature. A simple three-electrode cell was used in our experiments. A graphite electrode was used as a counter electrode (spectral grade, 1.8 cm^2). A saturated calomel electrode (SCE) with a double salt bridge system was used as the reference electrode that was connected to the cell. All potentials used in electrodeposition were the values *vs* SCE. A pure Ti plate (99.99%, 1.0 cm^2) was used as working electrode. Before electrodeposition, Ti substrate was cleaned ultrasonically in 0.1 M HCl, distilled water, and acetone and then rinsed in distilled water again.

The surface morphologies of Pd-Sn alloy nanosheet dendrites (ANSDs) were characterized by field emission scanning electron microscopy (FE-SEM, JSM-6330F) and transmission electron microscope (TEM, JEM-2010HR). The deposits were also characterized by X-ray diffraction (XRD, PIGAKU, D/MAX 2200 VPC) to determine deposit structures. Chemical-state analysis of deposits was carried out by X-ray photoelectron spectroscopy (XPS) using an ESCALAB 250 X-ray photoelectron spectrometer. All XPS spectra were corrected using the C 1s line at 284.6 eV. Curve fitting and background subtraction were accomplished.

The electrocatalytic properties of the fabricated Pd-Sn ANSDs were studied in a standard three-electrode cell at room temperature. The Pd-Sn ANSDs grown on Ti substrate served as working electrode. A Pt foil served as the counter electrode (1.0 cm × 1.5 cm). A saturated calomel electrode (SCE) with a double salt bridge system was used as the reference electrode, and the potentials used in this study were the values *vs* SCE. Cyclic voltammetry (CV) measurements were carried out on a CHI 660C electrochemical workstation (CH instruments, Inc.). Before CV measurements, the Pd-Sn ANSDs were cleaned again by sequentially washing with acetone, ethanol, and water to remove the stabilizing agents on the surfaces. CV curves were recorded between -0.80 and 0.20 V *vs* SCE at 50 mV/s. The chronoamperometric and chronopotentiometric curves were also measured by using a CHI 660C electrochemical workstation. For the above electrochemical tests of ethanol oxidation reactions, an aqueous solution containing 1.0 M C_2H_5OH + 1.0 M KOH was used. Prior to all experiments, the electrolyte solution was purged with high purity nitrogen gas for 60 min. All electrochemical measurements were carried out at room temperature.

1. Chen, M., Wu, B., Yang, J. & Zheng, N. Small-adsorbate assisted shape control of Pd and Pt nanocrystals. *Adv. Mater.* **24**, 862–879 (2012).
2. Zhou, Z.-Y., Huang, Z.-Z., Chen, D.-J., Wang, Q., Tian, N. & Sun, S.-G. High-index faceted platinum nanocrystals supported on carbon black as highly efficient catalysts for ethanol electrooxidation. *Angew. Chem. Int. Edit.* **49**, 411–415 (2010).
3. Oezaslan, M., Heggen, M. & Strasser, P. Size-dependent morphology of dealloyed bimetallic catalysts: linking the nano to the macro scale. *J. Am. Chem. Soc.* **134**, 514–524 (2012).
4. Gao, M.-R., Gao, Q., Jiang, J., Cui, C.-H., Yao, W.-T. & Yu, S.-H. A Methanol-tolerant cathode catalyst Pt/CoSe2 nanobelts for direct methanol fuel cell. *Angew. Chem. Int. Edit.* **50**, 4905–4908 (2011).
5. Wu, J., Zhang, J., Peng, Z., Yang, S., Wagner, F. T. & Yang, H. Truncated octahedral Pt_3Ni oxygen reduction reaction electrocatalysts. *J. Am. Chem. Soc.* **132**, 4984–4985 (2010).
6. Xia, B. Y., Ng, W., Wu, H. B., Wang, X. & Lou, X. W. Self-supported interconnected Pt nanoarchitectures as highly stable electrocatalysts for low-temperature fuel cells. *Angew. Chem. Int. Edit.* **51**, 7213–7216 (2012).
7. Lim, B., Kobayashi, H., Yu, T., Wang, J., Kim, M. J., Li, Z.-Y., Rycenga, M. & Xia, Y. Synthesis of Pd-Au Bimetallic Nanocrystals via Controlled Overgrowth. *J. Am. Chem. Soc.* **132**, 2506–2507 (2010).
8. Hong, J. W., Kim, D., Lee, Y. W., Kang, S. W. & Han, S. W. Atomic-distribution-dependent electrocatalytic activity of Au–Pd bimetallic nanocrystals. *Angew. Chem. Int. Ed.* **50**, 8876–8870 (2011).
9. Xu, C., Wang, H., Shen, P. K. & Jiang, S. P. Highly ordered Pd nanowire arrays as effective electrocatalysts for ethanol oxidation in direct alcohol fuel cells. *Adv. Mater.* **19**, 4256–4259 (2007).
10. Ksar, F., Surendran, G., Ramos, L., Keita, B., Nadjo, L., Prouzet, E., Beaunier, P., Hagége, A., Audonnet, F. & Remita, H. Palladium nanowires synthesized in hexagonal mesophases: application in ethanol electrooxid-ation. *Chem. Mater.* **21**, 1612–1617 (2009).
11. Bianchini, C. & Shen, P. K. Palladium-based electrocatalysts for alcohol oxidation in half cells and in direct alcohol fuel cells. *Chem. Rev.* **109**, 4183–4206 (2009).
12. Koenigsmann, C., Santulli, A. C., Sutter, E. & Wong, S. S. Ambient surfactantless synthesis, growth mechanism, and size-dependent electrocatalytic behavior of high-quality, single crystalline palladium nanowires. *ACS Nano* **5**, 7471–7487 (2011).
13. Hu, F. P., Wang, Z. Y., Li, Y. L., Li, C. M., Zhang, X. & Shen, P. K. Improved performance of Pd electrocatalyst supported on ultrahigh surface area hollow carbon spheres for direct alcohol fuel cells. *J. Power Sources* **177**, 61–66 (2008).
14. Xiao, L., Zhuang, L., Liu, Y., Lu, J. & Abruña, H. D. Activating Pd by morphology tailoring for oxygen reduction. *J. Am. Chem. Soc.* **131**, 602–608 (2009).
15. Koenigsmann, C., Santulli, A. C., Gong, K., Vukmirovic, M. B., Zhou, W.-P., Sutter, E., Wong, S. S. & Adzic, R. R. Enhanced electrocatalytic performance of processed, ultrathin, supported Pd-Pt core-shell nanowire catalysts for the oxygen reduction reaction. *J. Am. Chem. Soc.* **133**, 9783–9795 (2011).
16. Wang, L., Nemoto, Y. & Yamauchi, Y. Direct synthesis of spatially-controlled Pt-on-Pd bimetallic nanodendrites with superior electrocatalytic activity. *J. Am. Chem. Soc.* **133**, 9674–9677 (2011).
17. Cui, G., Song, S., Shen, P. K., Kowal, A. & Bianchini, C. First-principles considerations on catalytic activity of Pd toward ethanol oxidation. *J. Phys. Chem. C* **113**, 15639–15642 (2009).
18. Wei, T., Kumar, D., Chen, M. S., Luo, K., Axnanda, S., Lundwall, M. & Goodman, D. W. Vinyl acetate synthesis over model Pd−Sn bimetallic catalysts. *J. Phys. Chem. C* **112**, 8332–8337 (2008).
19. Xing, Y., Cai, Y., Vukmirovic, M. B., Zhou, W.-P., Karan, H., Wang, J. X. & Adzic, R. R. Enhancing oxygen reduction reaction activity via Pd-Au alloy sublayer mediation of Pt monolayer electrocatalysts. *J. Phys. Chem. Lett.* **1**, 3238–3242 (2010).
20. Tian, N., Zhou, Z.-Y., Yu, N.-F., Wang, L.-Y. & Sun, S.-G. Direct electrodeposition of tetrahexahedral Pd nanocrystals with high-index facets and high catalytic activity for ethanol electrooxidation. *J. Am. Chem. Soc.* **132**, 7580–7581 (2010).
21. Huang, X. Q., Tang, S. H., Mu, X. L., Dai, Y., Chen, G. X., Zhou, Z. Y., Ruan, F. X., Yang, Z. L. & Zheng, N. F. Freestanding palladium nanosheets with plasmonic and catalytic properties. *Nature Nanotech.* **6**, 28–32 (2011).
22. Sun, Z., Kim, J. H., Zhao, Y., Bijarbooneh, F., Malgras, V., Lee, Y., Kang, Y.-M. & Dou, S. X. Rational design of 3D dendritic TiO_2 nanostructures with favorable architectures. *J. Am. Chem. Soc.* **133**, 19314–19317 (2011).
23. Mohanty, A., Garg, N. & Jin, R. A universal approach to the synthesis of noble metal nanodendrites and their catalytic properties. *Angew. Chem. Int. Edit.* **49**, 4962–4966 (2010).
24. Tong, S., Xu, Y., Zhang, Z. & Song, W. Dendritic bimetallic nanostructures supported on self-assembled titanate films for sensor application. *J. Phys. Chem. C* **114**, 20925–20931 (2010).
25. Huang, D., Bai, X. & Zheng, L. Ultrafast preparation of three-dimensional dendritic gold nanostructures in aqueous solution and their applications in catalysis and SERS. *J. Phys. Chem. C* **115**, 14641–14647 (2011).
26. Patra, S., Viswanath, B., Barai, K., Ravishankar, N. & Munichandraiah, N. High-surface step density on dendritic Pd leads to exceptional catalytic activity for formic acid oxidation. *ACS Appl. Mater. Interfaces* **2**, 2965–2969 (2010).
27. Lim, B., Jiang, M., Camargo, P. H. C., Cho, E. C., Tao, J., Lu, X., Zhu, Y. & Xia, Y. Pd-Pt bimetallic nanodendrites with high activity for oxygen reduction. *Science* **324**, 1302–1305 (2009).
28. McShane, C. M. & Choi, K.-S. Photocurrent enhancement of n-Type Cu_2O electrodes achieved by controlling dendritic branching growth. *J. Am. Chem. Soc.* **131**, 2561–2569 (2009).
29. Min, Y., Moon, G. D., Kim, B. S., Lim, B., Kim, J.-S., Kang, C. Y. & Jeong, U. Quick. Controlled synthesis of ultrathin Bi_2Se_3 nanodiscs and nanosheets. *J. Am. Chem. Soc.* **134**, 2872–2875 (2012).

30. Wagner, C. D., Riggs, W. M., Davis, L. E., Moulder, J. F. & Muilenberg, G. E. *Handbook of X-Ray Photo-electron Spectroscopy, Perkin-Elmer Corporation Physical Electronics Division, Eden Prairie, MN*, 1979, 82.
31. Jerdev, D. I. & Koel, B. E. Oxidation of ordered Pt-Sn surface alloys by O_2. *Surf. Sci.* **492**, 106–114 (2001).
32. Casella, I. G. & Contursi, M. An Electrochemical and XPS study of the electrodeposited binary Pd-Sn catalyst: the electroreduction of nitrate ions in acid medium. *J. Electroana. Chem.* **588**, 147–154 (2006).
33. Zhi, C., Bando, Y., Tang, C., Kuwahara, H. & Golberg, D. Large-scale fabrication of boron nitride nanosheets and their utilization in polymeric composites with improved thermal and mechanical properties. *Adv. Mater.* **21**, 2889–2893 (2009).
34. Cui, C.-H., Li, H.-H., Yu, J.-W., Gao, M.-R. & Yu, S.-H. Ternary heterostructured nanoparticle tubes: a dual catalyst and its synergistic enhancement effects for O_2/H_2O_2 reduction. *Angew. Chem. Int. Ed.* **49**, 9149–9152 (2010).
35. Xu, X., Jia, J., Yang, X. & Dong, S. A templateless, surfactantless, simple electrochemical route to a dendritic gold nanostructure and its application to oxygen reduction. *Langmuir* **26**, 7627–7631 (2010).
36. Qin, Y., Song, Y., Sun, N. J., Zhao, N., Li, M. X. & Qi, L. M. Ionic liquid-assisted growth of single-crystalline dendritic gold nanostructures with a three-fold symmetry. *Chem. Mater.* **20**, 3965–3972 (2008).
37. Wang, L. & Yamauchi, Y. Facile synthesis of three-dimensional dendritic platinum nanoelectrocatalyst. *Chem. Mater.* **21**, 3562–3569 (2009).
38. Wang, Y., Nguyen, T., Liu, X. & Wang, X. Novel palladium-lead (Pd-Pb/C) bimetallic catalysts for electrooxidation of ethanol in alkaline media. *J. Power Sources* **195**, 2619–2622 (2010).

Acknowledgments

This work was supported by NSFC (51173212, 21073240, and 21273290), Fundamental Research Fund for the Central Universities (11lgzd14), Research Fund for New Star Scientist of Pearl River Science and Technology of Guangzhou (2011J2200057), and Open-End Fund of State Key Lab of Physical Chemistry of Solid Surfaces of Xiamen University (201113).

Author contributions

L. X. D., A. L. W. and Y. N. O. planned and performed the experiments, collected and analyzed the data, and wrote the paper. G. R. L. supervised the project, and conceived the experiments, analyzed the results and wrote the paper. Q. L., R. G. and Y.-X. T. helped with synthesis of the materials and collected the data. All authors discussed the results and commented on the manuscript.

Additional information

Supplementary information accompanies this paper at http://www.nature.com/scientificreports

Competing financial interests: The authors declare no competing financial interests.

How to cite this article: Ding, L.-X. *et al.* Hierarchical Pd-Sn Alloy Nanosheet Dendrites: An Economical and Highly Active Catalyst for Ethanol Electrooxidation. *Sci. Rep.* **3**, 1181; DOI:10.1038/srep01181 (2013).